Plasmonic Grating-Enabled Broadband Polarization-Sensitive Detection in Isotropic Bi_2O_2Se

Tianci Hu(胡天赐)[1,2,†], Lingyuan Kong(孔令圆)[2,†], Cai Luo(罗猜)[2], Yi Wang(王艺)[2], Peiye Yan(颜培烨)[2], Yan Liang(梁艳)[2], Nannan Hu(胡楠楠)[2], Jian Zhao(赵健)[2], Ziyi Fu(付子怡)[2], Enbo Gao(高恩博)[2], Weikang Fang(方伟康)[2], Peng Bao(鲍鹏)[2], Xizheng Ding(丁玺铮)[1,2], Zhixiang Yu(喻志祥)[2], Baoli Liu(刘宝利)[1], Syed M. Huzaif[1], Xiaofeng Fan(樊晓峰)[1,*], Yang Guo(郭阳)[2,3,*], Changzhi Gu(顾长志)[2,3,*]

[1]*Key Laboratory of Automobile Materials of MOE, College of Materials Science and Engineering, Jilin University, Changchun 130012, China*

[2]*Beijing National Laboratory for Condensed Matter Physics, Institute of Physics, Chinese Academy of Sciences, Beijing 100190, China*

[3]*School of Physical Sciences, CAS Key Laboratory of Vacuum Physics, University of Chinese Academy of Sciences, Beijing 100190, China*

[†]These authors contributed equally to this work.

[*]The e-mail addresses of corresponding authors: yangguo@iphy.ac.cn (Y. Guo); xffan@jlu.edu.cn (X. Fan); czgu@iphy.ac.cn (C. Gu)

ABSTRACT

Two-dimensional Bi_2O_2Se possesses high mobility and broadband absorption, yet its tetragonal symmetry prevents intrinsic polarization-sensitive detection. Here, we integrate one-dimensional Au gratings onto epitaxial Bi_2O_2Se films to break this in-plane isotropy. This metasurface enables polarization-selective localized surface plasmon resonance excitation, inducing anisotropic near-field enhancement and polarization-dependent photoresponse from 520 to 1060 nm. Critically, the enhanced photoresponse is consistent with Au-induced interfacial potential modulation that may assist carrier separation and collection, yielding millisecond response, responsivity of 27.7 mA/W at 520 nm, and detectivity of 1.59×10^{10} Jones. polarization extinction ratio reach ≥1.6 across the entire band. These results demonstrate that one-dimensional plasmonic structuring can impart polarization sensitivity to intrinsically isotropic epitaxial Bi_2O_2Se, enabling polarization-resolved photodetection at Broadband spanning the visible to near-infrared range.

Keywords: bismuth oxyselenide, polarization-sensitive photodetectors, broadband photodetection, plasmonic gratings, metasurfaces

PACS： 85.60.Gz, 73.20.Mf, 42.25.Ja, 73.50.Pz

INTRODUCTION

Photodetectors traditionally measure only light intensity. However, many modern applications, including target recognition, remote sensing, and biological imaging, require more than intensity alone.[1,2] Consequently, next-generation photodetectors are evolving toward multi-dimensional information detection, capturing spectral, phase, and polarization signatures simultaneously.[3] Among these, polarization carries unique contrast mechanisms. It reveals surface morphology, material anisotropy, and stress states, making polarization-sensitive detection indispensable.[4] Conventional polarization sensing relies on bulky, discrete optical elements such as polarizers, waveplates, and beam splitters placed before a separate photodetector.[5] This architecture severely limits system miniaturization and integration. Thus, on-chip integrated polarization-sensitive photodetectors have become a critical research direction. More broadly, nanostructure and material engineering have provided versatile routes for tailoring light–matter

interactions and photoinduced carrier dynamics in optoelectronic systems. For example, plasmonic nanocavities have enabled electrically driven nanoscale light emission, nonlinear optical materials have been exploited for passive Q-switched laser operation, and three-dimensional nanostructured photoelectrodes have been demonstrated to improve optical harvesting and photogenerated-carrier transport. [6-8]

Two-dimensional (2D) layered materials offer an attractive platform for on-chip polarization detection due to their atomic thickness, mechanical flexibility, strong light-matter interaction, and CMOS compatibility.[9–13] Ideally, 2D materials with intrinsically anisotropic crystal structures, such as orthorhombic or monoclinic systems, provide native polarization sensitivity. However, many high-performance 2D materials, including graphene, MoS_2,[14] and Bi_2O_2Se,[15] possess in-plane isotropic lattices, either tetragonal or hexagonal. This precludes direct polarization-dependent photoresponse. The key challenge is therefore how to introduce in-plane optical anisotropy without degrading their excellent electronic transport properties.

Bi_2O_2Se, or BOS exhibits high electron mobility of approximately 311 $cm^2 V^{-1} s^{-1}$, a moderate bandgap of about 0.8 eV,[16] broadband absorption from 400 to 1550 nm,[17] and outstanding air stability.[18] These properties make it ideal for high-performance photodetection.[19–21] Yet its tetragonal structure, which belongs to space group I4/mmm, renders it intrinsically in-plane isotropic.[22,23] Prior attempts to break this symmetry have used heterojunctions,[24] nanowires,[25] or surface reconstruction.[26] While these approaches have succeeded in introducing some polarization sensitivity, they face clear limitations. These include poor scalability,[27] narrow spectral bandwidth,[28] loss of electrostatic modulation,[29] or incompatibility with large-area integration.[30]

Given these limitations, we sought a different strategy that does not require modifying the material itself. Plasmonic structures have previously been integrated with two-dimensional materials to enhance optical absorption and photodetection, demonstrating the effectiveness of plasmonic resonances for improving light–matter interactions. [31–33] Here, we integrate one-dimensional (1D) Au gratings directly onto epitaxial Bi_2O_2Se films. The resulting device operates as a broadband polarization-sensitive photodetector from 520 nm to 1060 nm. It delivers millisecond response times, a maximum responsivity of 27.7 mA/W at 520 nm, and a specific

detectivity of 1.59×10^{10} Jones. Our work demonstrate a distinct route toward multiwavelength polarization detection in isotropic Bi_2O_2Se.

RESULTS AND DISCUSSION

Structural Design and Fabrication

Figure 1a illustrates the overall three-dimensional physical architecture of the device. The device adopts a bottom-up three-layer stacked design: an insulating $SrTiO_3$ substrate at the bottom, a high-quality epitaxial Bi_2O_2Se film with a thickness of ~10 nm in the middle serving as the photoactive channel, a highly ordered Au grating array integrated on top, and Au electrodes patterned at both ends of the channel. The material characterization is shown in Fig. S1. The Bi_2O_2Se crystal consists of positively charged $[Bi_2O_2]^{2+}$ layers and negatively charged $[Se]^{2-}$ layers stacked alternately along the c-axis, as shown in the right panel of Figure 1a. This highly symmetric tetragonal structure (space group I4/mmm) endows the material with excellent in-plane transport properties but also results in strict in-plane isotropy in the macroscopic continuous film. To break this symmetry bottleneck at the macroscopic optical level, we introduced a 1D metallic grating. The grating periodicity defines a privileged axis in the plane. Under normal incidence, transverse magnetic (TM) polarized light, with its electric field perpendicular to the grating strips, can couple to LSPRs, while transverse electric (TE) polarized light, with its electric field parallel to the strips, cannot.[33,34] This polarization-dependent coupling is the physical origin of the in plane optical symmetry breaking.

We performed systematic FEM simulations by varying the grating period P, width W, and height H (Figure 1b). Based on these simulations, we selected P = 510 nm, W = 300 nm, and H = 90 nm. Under these parameters, the LSPR mode is centered at ~767 nm (Figure 1c). The relatively broad linewidth of this resonance provides measurable field enhancement across our target wavelengths of 520 nm, 633 nm, and 1060 nm. Figure 1c presents the simulated broadband reflectance spectra from 500 nm to 1100 nm under TE and TM polarized illumination, which indicate strong polarization selective absorption. Under TM polarization, a clear reflectance dip appears around 767 nm, which originates from the excitation of the LSPR mode. In contrast, under TE polarization, the grating exhibits high reflectance with no such dip, as the incident electric field is parallel to the grating strips and cannot couple to the LSPR. This strong polarization dependence confirms the expected symmetry-breaking behavior.

To further reveal the microscopic origin of this absorption enhancement, we extracted the cross-sectional electric field distribution under TM polarized light at the resonance wavelength of 767 nm, as shown in Figure 1d. The simulation results clearly demonstrate that high-intensity electric fields ($|E|^2/|E_0|^2$) are tightly confined within a minimal region at the interface between the bottom of the metallic grating and the Bi_2O_2Se film, forming strong LSPR hotspots.[35] Although the simulated resonance is centered at 767 nm, the broadband nature of the plasmonic mode ensures substantial field enhancement extending to both shorter and longer wavelengths, covering our experimental measurement range of 520 nm to 1060 nm. This polarization-dependent near-field localization at the metal-semiconductor interface successfully breaks the intrinsic optical symmetry of the system and provides the foundation for polarization-sensitive photodetection. Polarization-resolved reflection spectra were further measured for the fabricated device (Fig. S16). The experimental TE and TM spectra exhibit similar overall spectral evolution over a large part of the measured range, but show a pronounced difference in line shape within approximately 550–900 nm. In particular, a broad reflection depression appears under TM polarization, whereas the TE spectrum remains relatively smooth in this region. This polarization-dependent spectral contrast qualitatively supports the polarization-selective optical response predicted by the simulations. The remaining differences in resonance position, linewidth, and absolute reflectance between experiment and simulation are attributed to fabrication-induced structural variations, material-parameter uncertainties, and experimental spatial/angular averaging.

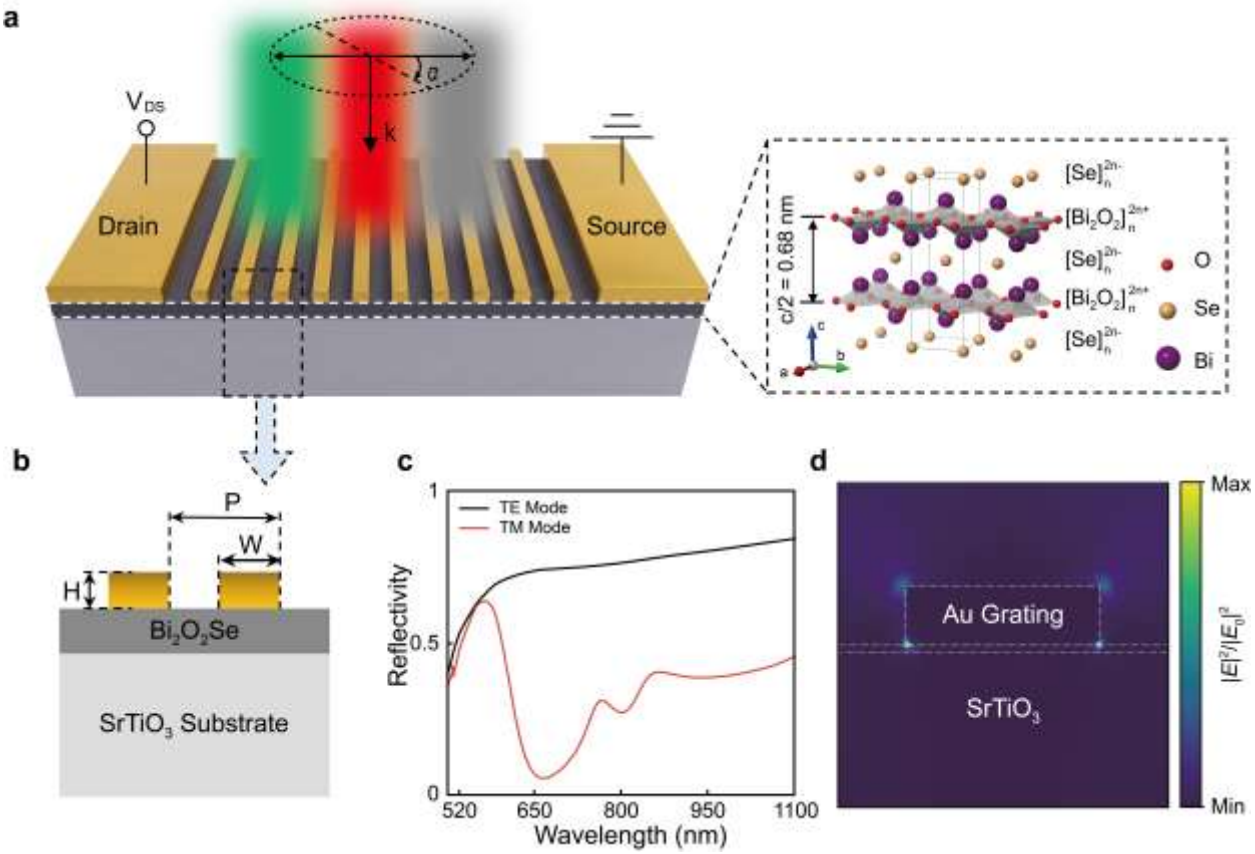


Figure 1. Structural design and plasmonic mechanism of the grating-enhanced Bi_2O_2Se photodetector. (a) Device architecture (left) and Bi_2O_2Se crystal structure (right). (b) Cross-sectional geometry of the Au grating. (c) Simulated reflectance spectra under TE and TM polarization. The deep dip under TM illumination indicates strong polarization-selective absorption. (d) Simulated electric field enhancement at the metal/Bi_2O_2Se interface under TM excitation at 767 nm. The highly confined fields reveal LSPR hotspots.

Based on the above design, we fabricated the grating-enhanced photodetector using an electron beam lithography (EBL)-based micro-nano fabrication process, as illustrated in Figure 2a. The process primarily included: spin-coating PMMA photoresist onto the MBE-grown Bi_2O_2Se film, EBL patterning, electron beam evaporation deposition of Ti/Au (5 nm/85 nm), and final metal lift-off. Figure 2b presents a large-area SEM image of the fabricated metasurface photodetector. The dense and uniform Au grating array is free of obvious breakages or metal bridging. The high-magnification SEM image in the inset of Figure 2b further confirms that the actual fabricated

grating period (P = 510 nm) and metal strip width (W = 300 nm) agree well with the theoretical design parameters, demonstrating the high fidelity of this fabrication process.

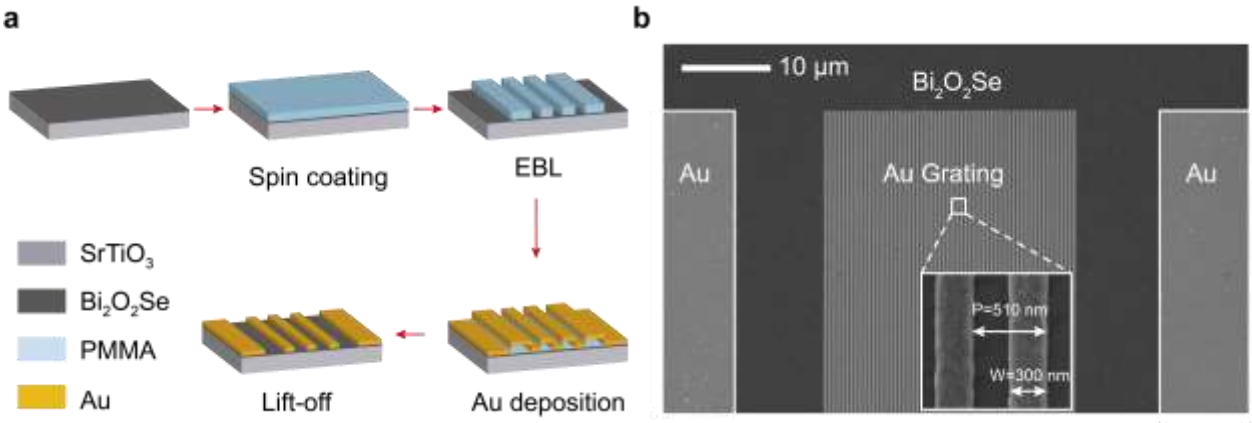


Figure 2. Fabrication process and morphology of the grating-enhanced photodetector. (a) Schematic of the micro-nanofabrication process using electron beam lithography (EBL) and electron beam evaporation. (b) Large-area SEM image of the fabricated device. The inset shows a high-magnification view. The grating period and width match the design values, confirming high fabrication fidelity.

Photoresponse Performance

To systematically evaluate the impact of the plasmonic grating on device performance, we performed comparative optoelectronic measurements on Bi_2O_2Se detectors with and without gratings. Figure 3a presents the I-V characteristics of the devices under dark conditions and 633 nm illumination (P_{in}=5 μW) across a bias range of ±10 V. Additional wavelength-dependent I–V characteristics are provided in Fig. S2. Under dark conditions, the grating-integrated device exhibits a dark current of approximately 0.1 nA(100 pA) at -10 V, which is two orders of magnitude higher than that of the pristine device (~0.5 pA). We attribute this increase to additional interfacial states introduced during Au deposition, is consistent with the rectifying I-V characteristics (Figure 3a). Despite this increase, the absolute dark current remains in the sub-nanoampere regime (100 pA), which is sufficiently low for high-detectivity operation. This slight penalty is a worthwhile trade-off given the substantial gain in photoresponse and polarization sensitivity. Moreover, the grating-integrated device shows asymmetric rectification characteristics in its I-V curve, indicating that the introduction of periodic Au/Bi_2O_2Se interfaces modifies the carrier transport behavior

within the channel. Upon illumination, the photocurrent of the grating-integrated device increases by nearly three orders of magnitude compared with its pristine counterpart.

The enhanced photocurrent can be understood as arising from the combined optical and interfacial effects introduced by the Au grating. First, the localized surface plasmon resonance concentrates the electromagnetic field near the Au/Bi_2O_2Se interface, thereby enhancing photocarrier generation in the Bi_2O_2Se layer. In addition, Au deposition can induce interfacial charge redistribution and locally modify the carrier density and electrostatic potential of Bi_2O_2Se. [36-38] The Au-modified region can therefore be phenomenologically regarded as an electron-rich n^+-like Bi_2O_2Se region relative to the surrounding n-type channel, giving rise to local band bending and an n^+/n-like built-in potential near the grating edges.[39] Such local potential modulation can assist the separation and collection of photogenerated carriers. We employ the classic Debye screening length formula to estimate the characteristic spatial scale of this modulation. The calculated characteristic screening length is approximately 7.5 nm, comparable to the thickness of Bi_2O_2Se; we also present a schematic diagram of the band bending. (the detail analysis see Fig. S9)

To further investigate the carrier collection process and its impact on photocurrent generation, we extracted the power-dependent net photocurrent at a reverse bias of -10 V under 1060 nm illumination, following the relationship $I_{ph} \propto P_{in}^{\theta}$, as shown in Figure 3b. Additional power-dependent photocurrent fittings are provided in Fig. S3. The fitting slope for the pristine device is $\theta = 0.73$, indicating considerable carrier recombination and trapping processes. For the grating-integrated device, $\theta = 0.96$, which is close to the ideal value of 1.0. This near-unity exponent is consistent with efficient carrier collection under reverse bias. The result suggests that the grating-induced interface fields promote carrier separation and extraction before recombination occurs, leading to a nearly linear dependence of photocurrent on incident optical power.[20]

Figure 3c further compares the responsivity (R) of the devices across a broad visible to near-infrared spectrum (520 nm, 633 nm, and 1060 nm). The responsivity R is calculated by the following equation: $R=(I_{light}-I_{dark})/P_{in}$, where I_{light} is the device current under illumination, I_{dark} represents the dark current, and P_{in} denotes the total incident optical power on the effective area of the device.[19] Across the entire tested power range, the responsivity of the grating-integrated device exceeds that of the control group by three orders of magnitude. Such a substantial

enhancement is consistent with the combined contributions of plasmon-enhanced photocarrier generation and improved carrier collection associated with Au-induced interfacial potential modulation.

Moreover, we evaluated the dynamic characteristics of the devices under manual optical switching modulation. The time-response curves under 633 nm shown in Figure 3d confirm superior cyclic stability. Notably, the grating-integrated device exhibits a faster response time (<10 ms) than the pristine counterpart (see Fig. S4 for details). This observation further supports the conclusion that the enhanced photoresponse originates from more efficient carrier separation and extraction rather than from a trap-dominated gain mechanism, which typically leads to prolonged response dynamics.[14] The device shows a sharper rising edge upon illumination, accompanied by a distinct transient overshoot peak. The device shows a sharp transient overshoot immediately after illumination is switched on. This feature is attributed to a transient photothermal/pyroelectric-like contribution induced by the rapid light-induced temperature variation. As the device approaches thermal equilibrium, the transient component decays and the current reaches a steady-state value. The decay following the overshoot approximately follows $(I \propto t^{-0.5})$, consistent with a heat-diffusion-mediated transient response (see Fig. S5 for details).[40]

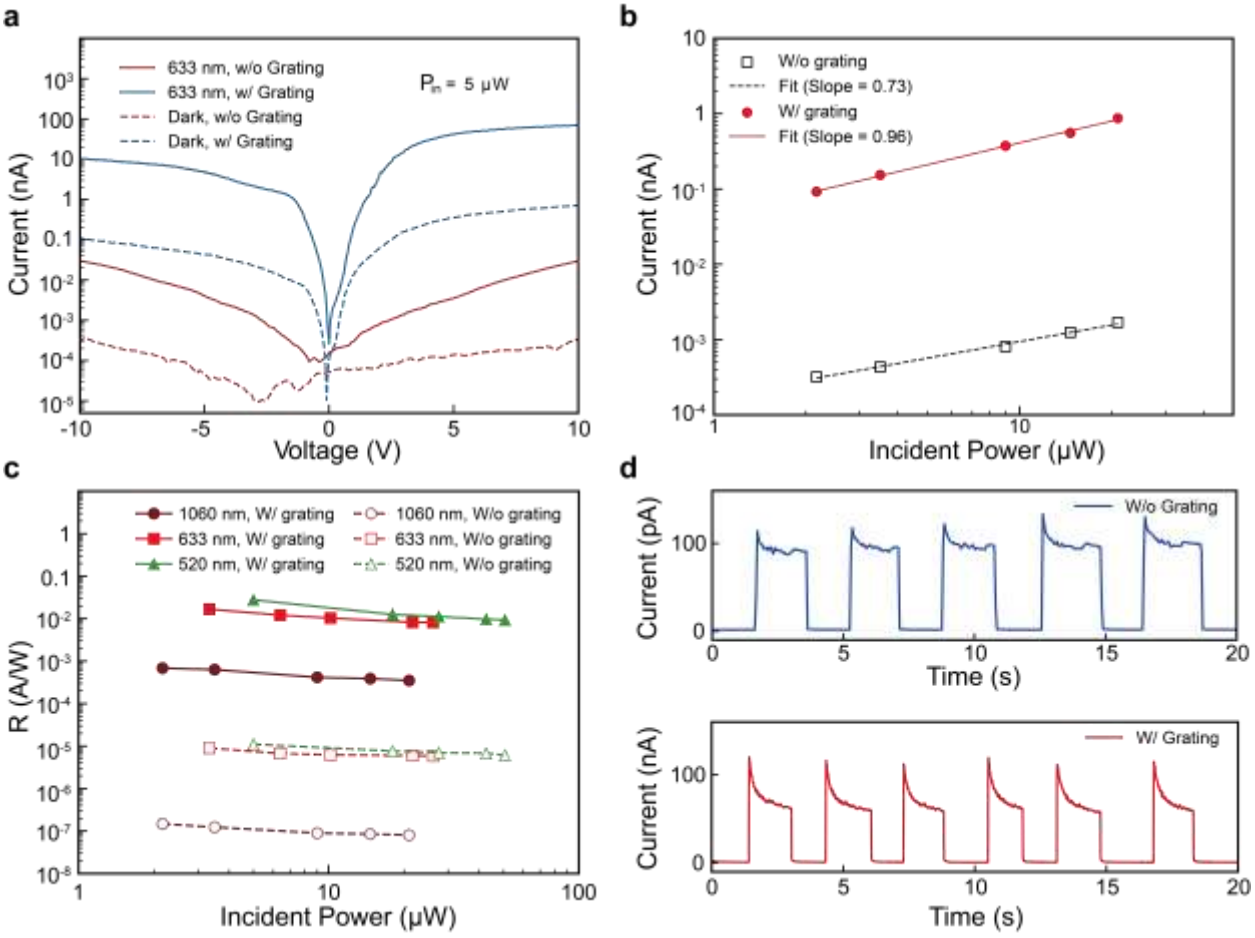


Figure 3. Optoelectronic performance of the grating-enhanced Bi_2O_2Se photodetector. (a) I–V curves under dark conditions and 633 nm illumination for devices with and without Au gratings. The current magnitude is plotted in nA on a logarithmic scale. (b) Photocurrent versus incident power at −10 V under 1060 nm. The near-unity slope ($\theta = 0.96$) indicates efficient carrier extraction with minimal trap-assisted recombination. (c) Broadband responsivity as a function of incident optical power at 520, 633, and 1060 nm under V_{DS} = 10 V. The maximum responsivities of 27.7, 16.7, and 0.68 mA W^{-1} at 520, 633, and 1060 nm were obtained at the lowest incident powers of 5.0, 3.3, and 2.1 μW, respectively. (d) Transient photocurrent response under 633 nm illumination. The transient overshoot at light switching is associated with a rapid photothermal/pyroelectric-like response, followed by relaxation toward the steady-state photocurrent.

We further tested the comprehensive core optoelectronic metrics of the metasurface-integrated detector to evaluate its practical application potential in broadband detection, with the key parameters summarized in Table 1. The results show that the rise time (τ_{rise}) and decay time

(τ_{decay}) of the device under 633 nm excitation are approximately 4.0 ms and 14.5 ms, respectively. Here, τ_{rise} and τ_{decay} are defined as the time intervals required for the photocurrent to increase from 10% to 90% and to decrease from 90% to 10% of its peak steady-state value, respectively.[20] At 1060 nm, both rise (83.9 ms) and decay (246.4 ms) times increase by roughly one order of magnitude compared to visible wavelengths. This degradation is attributed to the reduced photon energy in the near-infrared, which lowers carrier generation efficiency and reduces the effective signal-to-noise ratio, leading to slower measurable transient dynamics. The local band bending and interfacial potential modulation associated with the Au-modified Bi_2O_2Se region may facilitate carrier separation and extraction under reverse bias, contributing to the observed millisecond-scale response.

Beyond speed, the device exhibits excellent sensitivity and signal discriminability. The maximum optical switching ratio (I_{light}/I_{dark}) of the device reaches 1346 at a wavelength of 520 nm under a -10 V bias. To comprehensively evaluate the device's ability to detect weak optical signals, we systematically summarized the maximum responsivity (R) and specific detectivity (D^*) of the device at different incident wavelengths. The specific detectivity D^* is the core metric for measuring the intrinsic sensitivity of a detector, which is calculated using the following equation (assuming shot noise is the dominant noise source): $D^* = \frac{RA^{1/2}}{(2eI_{dark})^{1/2}}$ where R is the responsivity, A is the effective illumination area of the device, e is the elementary charge (1.602×10^{-19} C), and I_{dark} is the dark current.[41] Empowered by the dual advantages of plasmonic optical near-field confinement and electrical amplification, the device exhibits exceptional detection sensitivity in the visible light band. Particularly under 520 nm excitation, both R and D^* reach their maximum values of 27.7 mA/W and 1.59×10^{10} Jones, respectively. More importantly, even in the near-infrared band at 1060 nm, the device maintains effective broadband photoelectric conversion. These precisely quantified comprehensive performance metrics demonstrate that by integrating a 1D plasmonic metal grating, we have successfully constructed a high-performance 2D optoelectronic detection platform featuring high responsivity, fast speed, low noise, and broadband coverage.

Wavelength (nm)	Rise / Decay Time (ms)	On/off Ratio	Rmax(mA/W)	Detectivity D* (Jones)
1060	83.9/246.4	9	0.68	3.9×10^{8}
633	4/14.5	615	16.7	9.5×10^{9}
520	3/48.6	1346	27.7	1.59×10^{10}

Table 1. Comprehensive broadband optoelectronic performance of the metasurface-integrated Bi_2O_2Se photodetector. The maximum responsivities listed in the table were obtained at V_{DS} = 10 V. The corresponding incident powers were 2.1, 3.3, and 5.0 μW for 1060, 633, and 520 nm, respectively.

To evaluate device-to-device reproducibility, ten grating-integrated Bi_2O_2Se photodetectors fabricated on the same wafer were statistically characterized under identical conditions. At 633 nm, the devices exhibit an average dark current of approximately 0.41 ± 0.03 nA, an average responsivity of approximately 15.5 ± 1.5 mA W^{-1}, and an average polarization extinction ratio of approximately 1.48 ± 0.12. In addition, the device maintains a comparable switching photoresponse after three month of storage under ambient conditions, demonstrating good environmental stability. Continuous-illumination measurements further confirm that the device retains a measurable and stable photoresponse under prolonged optical excitation (see Fig. S13 and Fig. S14 for details). These results indicate reasonable device-to-device reproducibility and operational stability of the grating-integrated Bi_2O_2Se photodetectors.

Broadband Polarization-Resolved Photoresponse Characteristics

After confirming that the plasmonic metasurface can significantly enhance the photoresponsivity, we further evaluated the modulation effect of this 1D grating on the polarization-sensitive detection capabilities of the device. Figure 4 presents spolar plots of the photoresponsivity as a function of the incident light polarization angle (α) under various wavelengths. First, we performed polarization-resolved measurements on the pristine control device without gratings (Figure 4a–c). Under laser excitation at 520 nm, 633 nm, and 1060 nm, the polar plots of the control device all exhibit nearly perfect circular distributions. This experimental result indicates that the intrinsic Bi_2O_2Se channel is insensitive to the polarization state of the incident light, perfectly corroborating the materials characterization in Figure 1 regarding the in-plane isotropic lattice structure of its tetragonal system (space group I4/mmm).

Subsequently, we tested the device integrated with Au gratings (Figure 4d–f). The polarization-dependent photoresponse of the device can be described by the equation: $I_{ph}[\alpha]=I_{max}\,cos^2(\alpha-\varphi)+I_{min}\,sin^2(\alpha-\varphi)$, where $I_{ph}[\alpha]$ is the total photocurrent as a function of the polarization angle α, defined as the rotation angle of the incident polarization direction relative to the grating strips; φ is the azimuthal offset angle that defines the orientation of the detector's maximum-response axis in the laboratory frame; I_{max} and I_{min} denote the maximum and minimum photocurrents, respectively.[33] In stark contrast to the control group, the polar response plots of the grating-integrated device exhibit a highly anisotropic "dumbbell-like" or elliptical distribution. This polarization dependence originates directly from the 1D grating, which breaks the in-plane optical symmetry of the device system. In general, particularly around the plasmonic resonance and at 633 nm, TM-polarized illumination produces stronger localized fields near the grating edges than TE polarization, leading to enhanced absorption in the Bi_2O_2Se layer. However, the polarization dependence is wavelength dependent rather than universally TM dominated over the entire spectral range.

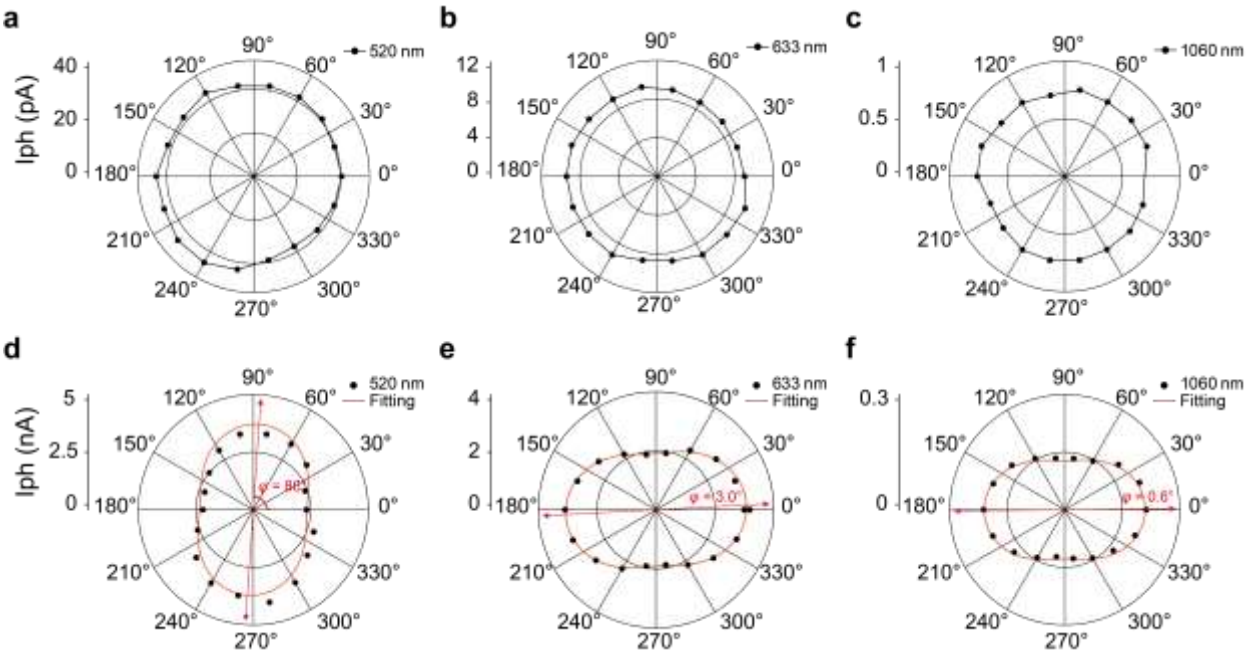


Figure 4. Broadband polarization-resolved photoresponse characteristics of the photodetector. (a-c) Polar plots of the responsivity for the devices without gratings at 520 nm, 633 nm, and 1060 nm. The circular response distribution confirms the in-plane isotropy of intrinsic Bi_2O_2Se. (d-f) Polar

plots for the grating-integrated device at the same wavelengths. The elliptical or dumbbell-like distributions demonstrate strong polarization anisotropy.

Notably, this optical anisotropy induced by the artificial micro-nanostructure is not confined to a single resonant wavelength but spans a broad spectral range from the visible (520 nm, 633 nm) to the near-infrared (1060 nm). The polarization sensitivity was quantitatively evaluated using the polarization extinction ratio (PER), defined as (I_{max}/I_{min}) device exhibits PER values of approximately 1.6, 1.7, and 1.6 at 520, 633, and 1060 nm, respectively. In addition, the PER remains within approximately 1.37–1.77 over the investigated power ranges without pronounced degradation at higher optical power (Fig. S12), indicating that the steady-state polarization anisotropy is not dominated by high-power saturation or transient pyroelectric effects.

The comparison of representative performance metrics of Bi_2O_2Se-based polarization-sensitive PDs can be seen in Table 2. The polarization-dependent data at 520 nm show relatively larger deviations from the ideal fitting than those at 633 and 1060 nm, which are likely associated with experimental fluctuations during the angular scan, including residual laser-power fluctuations and minor variations in optical alignment. Nevertheless, the overall anisotropic polarization dependence remains clearly resolved.

At 520 nm, the maximum-response axis rotates by approximately 86° relative to that at longer wavelengths, resulting in $(I_{\mathrm{TE}} > I_{\mathrm{TM}})$. To clarify the origin of this inversion, we further examined the surface-mode dispersion, electromagnetic field distribution, and thin-film interference. For the Au/Bi_2O_2Se interface, the calculated effective SPP index at 520 nm is $(\mathrm{Re}(n_{\mathrm{eff}}) \approx 0.91)$, whereas first-order grating coupling requires $(\lambda/P \approx 1.02)$, indicating that efficient coupling to a propagating Au/Bi_2O_2Se SPP is not satisfied. Consistently, the field distribution at 520 nm is dominated by localized edge fields rather than a characteristic propagating SPP mode. In addition, thickness-dependent calculations show nearly identical TE and TM spectral evolution for the planar Bi_2O_2Se film, excluding conventional thin-film interference as the origin of the polarization reversal. Instead, the inversion originates from the wavelength-dependent redistribution of the optical field induced by the Au grating: at 520 nm, the layer-resolved absorption of Bi_2O_2Se is larger under TE polarization, whereas TM absorption dominates at 633 and 1060 nm (Fig. S6).

Device	Symmetry-breaking Strategy	Wavelength (nm)	Polarization Ratio	Responsivity (A/W)	D*(Jones)
$Bi_2O_2Se/MoSe_2$[22]	1D Geometry	635(single)	2.2	17.17	1.21×10^{11}
Bi_2O_2Se/WSe_2 [23]	Surface Reconstruction	405, 635(double)	2.2, 4.9	44	3.1×10^{13}
ReS_2/Bi_2O_2Se [21]	3D Heterojunction	850(single)	1.4	3.4	1.0×10^{10}
Bi_2O_2Se film	1D Au Grating	520, 633, 1060	1.6, 1.7, 1.6	0.0277	1.59×10^{10}

Table 2. Comparison of representative performance metrics of Bi_2O_2Se-based polarization-sensitive photodetectors.

CONCLUSIONS

In summary, we have demonstrated a multiwavelength polarization-sensitive photodetector by coupling 1D plasmonic Au gratings with epitaxial 2D Bi_2O_2Se continuous films. The enhanced photoresponse is also consistent with interface-induced potential modulation that may facilitate carrier separation and extraction. Consequently, the device achieves a detectivity of 1.59×10^{10} Jones, a light-to-dark switching ratio of $> 10^3$, and millisecond-level response at 520, 633, and 1060 nm. The realization of broadband Empowered by the dual advantages of polarization ratios up to 1.7 confirms that our plasmonic interface engineering effectively overcomes the intrinsic isotropic limitations of Bi_2O_2Se. This approach provides a lithographically defined approach for integrating polarization sensitivity into isotropic Bi_2O_2Se photodetectors, and paves a highly compatible and scalable pathway for developing next-generation integrated, multifunctional optoelectronic systems.[13]

EXPERIMENTAL SECTION

Device Fabrication. The BOS thin films were deposited on insulating $SrTiO_3$ substrates using molecular beam epitaxy (MBE). Subsequently, a poly(methyl methacrylate) (PMMA-495A5) electron-beam resist was spin-coated onto the sample and baked on a hot plate at 180 °C for 1 min. This was followed by the spin-coating of a conductive layer (anti-charging layer), which was baked at 90 °C for 1 min. The gratings and electrodes were then patterned using electron-beam lithography (EBL, JBX-6300FS). After exposure, the surface conductive layer was rinsed off with deionized water. The samples were then developed in a developer solution for 40 s and fixed in a stopper solution for 30 s. Following this, a 5 nm Ti / 85 nm Au metal film was deposited via electron-beam evaporation (EBE). Finally, a standard lift-off process was performed to yield the patterned Au grating and electrode structures.

Numerical Simulation. Numerical finite element method (FEM) simulations were performed using COMSOL Multiphysics to calculate the optical spectra and local electric field distributions of the devices. In our simulations, periodic boundary conditions were applied along the periodicity direction, and perfectly matched layer (PML) boundary conditions were applied along the light propagation direction. A normally incident plane wave was utilized as the optical excitation source. All data were extracted after ensuring the computational convergence of the simulations.

Optoelectronic Measurements. The electrical and optoelectronic characteristics of the devices were evaluated using a probe station equipped with a semiconductor parameter analyzer (4200-SCS, Keithley). All optoelectronic measurements were performed on a custom-built optical platform. For polarization-resolved photocurrent measurements, a linear polarizer was used to define the initial polarization state of the incident laser. The polarization angle was systematically tuned by rotating a half-wave plate, thereby varying the polarization state without intentionally changing the incident optical power. Minor temporal fluctuations of the laser output may nevertheless contribute to the experimental uncertainty during the angular scan.

ASSOCIATED CONTENT

Supporting Information.

Morphology and structural characterization of epitaxial Bi_2O_2Se films; supplementary wavelength-dependent optoelectronic characteristics; transient photoresponse measurements;

analysis of the transient pyroelectric effect; polarization-dependent absorption simulations; optical setup for photoelectric characterization; and simulated electric-field distributions of the plasmonic metasurface. (PDF)

AUTHOR INFORMATION

Corresponding Authors

Yang Guo — *Beijing National Laboratory for Condensed Matter Physics, Institute of Physics, Chinese Academy of Sciences, Beijing 100190, China; School of Physical Sciences, CAS Key Laboratory of Vacuum Physics, University of Chinese Academy of Sciences, Beijing 100190, China;* Email: yangguo@iphy.ac.cn

Xiaofeng Fan — *Key Laboratory of Automobile Materials of MOE, College of Materials Science and Engineering, Jilin University, Changchun 130012, China;* Email: xffan@jlu.edu.cn

Changzhi Gu — *Beijing National Laboratory for Condensed Matter Physics, Institute of Physics, Chinese Academy of Sciences, Beijing 100190, China; School of Physical Sciences, CAS Key Laboratory of Vacuum Physics, University of Chinese Academy of Sciences, Beijing 100190, China;* Email: czgu@iphy.ac.cn

Author Contributions

†T. Hu and L. Kong contributed equally to this work. The manuscript was written through contributions of all authors. All authors have given approval to the final version of the manuscript.

Funding Sources

This work was supported by the National Key Research and Development Program of China under Grant Nos. 2024YFA1207700; National Natural Science Foundation of China under Grants Nos. 92265110, 62174179. Natural Science Foundation of Jilin Province, China under Grant No.

20240101320JC. This work was also supported by the Micro/nano Fabrication Laboratory of Synergetic Extreme Condition User Facility (SECUF).

Notes

The authors declare no competing financial interest.

ACKNOWLEDGMENT

This work was supported by the National Key Research and Development Program of China under Grant Nos. 2024YFA1207700; National Natural Science Foundation of China under Grants Nos. 92265110, 62174179. Natural Science Foundation of Jilin Province, China under Grant No. 20240101320JC. This work was also supported by the Micro/nano Fabrication Laboratory of Synergetic Extreme Condition User Facility (SECUF).

REFERENCES

[1] Ha S T, Li Q, Yang J K W, Demir H V, Brongersma M L and Kuznetsov A I 2024 *Science* 386 eadm7442

[2] Han J, Fu Z, Wei J, Han S, Deng W, Hu F, Wang Z, Zhou H, Yu H, Gou J and Wang J 2025 *Light Sci. Appl*. 14 362

[3] Liu M, Qi L, Zou Y, Zhang N, Zhang F, Xiang H, Liu Z, Qin M, Sun X, Zheng Y, Lin C, Li D and Li S 2025 *Nat. Commun*. 16 2774

[4] Wu D, Guo J, Du J, Xia C, Zeng L, Tian Y, Shi Z, Tian Y, Li X J, Tsang Y H and Jie J 2019 *ACS Nano* 13 9907–17

[5] Wilson N C, Shin E, Bangle R E, Nikodemski S B, Vella J H and Mikkelsen M H 2023 *Nano Lett*. 23 8547–52

[6] L. Sun, J. Li, J. Han, Y. Lu, M. Meng, B. Li, M. Jiang, *Opt. Laser Technol*. 2025, 181, 112038.

[7] Q. Zhu, L. Yu, B. Wen, J. Cheng, Y. Deng, J. Li, *Opt. Quantum Electron*. 2024, 56, 1032.

[8] M. Meng, N. Qin, L. Sun, Y. Chen, K. Xu, Y. Zhang, M. Liu, S. Du, K. Liu, Y. Feng, G. Wang, H. Yuan, J. *Nanoelectron. Optoelectron*. 2021, 16, 1342.

[9] Wang Z, Chen J, Zhu J, Batool H S, Hu J and Wang D 2026 *Langmuir* 42 10798–813

[10] Liang Y, Chen Y, Sun Y, Xu S, Wu J, Tan C, Xu X, Yuan H, Yang L, Chen Y, Gao P, Guo J and Peng H 2019 *Adv. Mater.* 31 1901964

[11] Jiang H, Chen Y, Guo W, Zhang Y, Zhou R, Gu M, Zhong F, Ni Z, Lu J, Qiu C-W and Gao W 2024 *Nat. Commun.* 15 8347

[12] Deng J, Shi M, Liu X, Zhou J, Qin X, Wang R, Zhen Y, Dai X, Chen Y, Wei J, Ni Z, Gao W, Qiu C-W and Chen X 2024 *Nat. Electron.* 7 1004–14

[13] Kong L, Li W, Wang Z, Fan Z, Yin Z, Ling H, Hu K, Tai S, Li D, Li C, Guo Y, Yang F, Zhang W, Guo J, Xu R, Chen P, Liang Y and Zhang J 2025 *Adv. Mater.* 37 e10566

[14] Syong W-R, Fu J-H, Kuo Y-H, Chu Y-C, Hakami M, Peng T-Y, Lynch J, Jariwala D, Tung V and Lu Y-J 2024 *ACS Nano acsnano*.3c10390

[15] Yin J, Tan Z, Hong H, Wu J, Yuan H, Liu Y, Chen C, Tan C, Yao F, Li T, Chen Y, Liu Z, Liu K and Peng H 2018 *Nat. Commun.* 9 3311

[16] Kong L, Li W, Hu K, Fan Z, Yin Z, Ling H, Wang Z, Li D, Tai S, Li C, Jabeen F, Guo Y, Xu R, Yang F, Guo J, Zhang W, Chen P, Liang Y and Zhang J 2025 *Nano Lett*. 25 17636–43

[17] Lakhchaura S, Gokul M A and Rahman A 2024 *Nanotechnology* 35 075707

[18] Tao H, Wang T, Li D, Xing J and Li G 2023 *J. Semicond*. 44 031001

[19] Xue X, Ling C, Ji H, Wang J, Wang C, Lu H and Liu W 2023 *ACS Appl. Mater. Interfaces* 15 5411–9

[20] Tong T, Chen Y, Qin S, Li W, Zhang J, Zhu C, Zhang C, Yuan X, Chen X, Nie Z, Wang X, Hu W, Wang F, Liu W, Wang P, Wang X, Zhang R and Xu Y 2019 *Adv. Funct. Mater*. 29 1905806

[21] Yang H, Tan C, Deng C, Zhang R, Zheng X, Zhang X, Hu Y, Guo X, Wang G, Jiang T, Zhang Y, Peng G, Peng H, Zhang X and Qin S 2019 *Small* 15 1904482

[22] Huang X, Niu C-Y, Zhang J, Wang A, Jia Y and Song Y 2019 *APL Mater*. 7 081110

[23] Tian H, Tice J, Fei R, Tran V, Yan X, Yang L and Wang H 2016 *Nano Today* 11 763–77

[24] Gou J, Yang X, Yu H, Yu H, Wei Y, Fu Z, Wei L, Wang Z, Han J, Wu Z, Jiang Y and Wang J 2025 *Laser Photonics Rev*. 19 2500577

[25] Chen Z, Huang J, Yang M, Liu X, Zheng Z, Huo N, Han L, Luo D, Li J and Gao W 2023 *ACS Appl. Mater. Interfaces* 15 30504–16

[26] Tao L, Li S, Yao B, Xia M, Gao W, Yang Y, Wang X and Huo N 2021 *ACS Omega* 6 34763–70

[27] Cai Z, Liu B, Zou X and Cheng H-M 2018 *Chem. Rev.* 118 6091–133

[28] Zhou X, Hu X, Yu J, Liu S, Shu Z, Zhang Q, Li H, Ma Y, Xu H and Zhai T 2018 *Adv. Funct. Mater.* 28 1706587

[29] Frisenda R, Navarro-Moratalla E, Gant P, Pérez De Lara D, Jarillo-Herrero P, Gorbachev R V and Castellanos-Gomez A 2018 *Chem. Soc. Rev.* 47 53–68

[30] Barrigón E, Heurlin M, Bi Z, Monemar B and Samuelson L 2019 *Chem. Rev.* 119 9170–220

[31] Wei J, Li Y, Wang L, Liao W, Dong B, Xu C, Zhu C, Ang K-W, Qiu C-W and Lee C 2020 *Nat. Commun.* 11 6404

[32] Lu X, Jiang P and Bao X 2019 *Nat. Commun.* 10 138

[33] Lien M R, Wang N, Wu J, Soibel A, Gunapala S D, Wang H and Povinelli M L 2022 *Nano Lett.* 22 8704–10

[34] Zhang X, Yu Y, Cui Y, Yang F, Wang W, Liu L, Lu J and Ni Z 2022 *Appl. Phys. Lett.* 121 061103

[35] Bai Q, Huang X, Guo Y, Du S, Sun C, Hu L, Zheng R, Yang Y, Jin A, Li J and Gu C 2023 *Nano Res*. 16 10272–8

[36] Chen H-T, Taylor A J and Yu N 2016 *Rep. Prog. Phys.* 79 076401

[37] Yao Y, Shankar R, Rauter P, Song Y, Kong J, Loncar M and Capasso F 2014 *Nano Lett.* 14 3749–54

[38] Liu Y, Guo J, Zhu E, Liao L, Lee S-J, Ding M, Shakir I, Gambin V, Huang Y and Duan X 2018 *Nature* 557 696–700

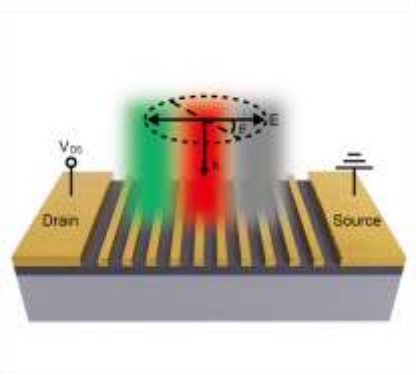
[39] Youn S and Chang J 2023 *Adv. Electron. Mater*. 9 2201221

[40] Guo Y, Song Y, Yang M, Xu Z, Xie H, Li H, Li Z, Liang H, Ruan S and Zeng Y-J 2020 *J. Mater. Chem. C* 8 13226–34

[41] Lan H-Y, Hsieh Y-H, Chiao Z-Y, Jariwala D, Shih M-H, Yen T-J, Hess O and Lu Y-J 2021 *Nano Lett*. 21 3083–91

Table of Contents

Plasmonic Grating-Enabled Broadband Polarization-Sensitive Detection in Isotropic Bi_2O_2Se



A one-dimensional Au grating is integrated with epitaxial Bi_2O_2Se to break its intrinsic in-plane optical isotropy. The plasmonic interface enables polarization-selective near-field enhancement and efficient carrier extraction, producing broadband polarization-sensitive photodetection from 520 to 1060 nm with millisecond response, high detectivity, and scalable device integration.